# Ganymede s internal structure including thermodynamics of magnesium sulfate oceans in contact with ice

Steve Vance, Mathieu Bouffard, Mathieu Choukroun, Christophe Sotin

Planetary and Space Science 96 (2014) 62–70

Contents lists available at ScienceDirect

Planetary and Space Science

journal homepage: www.elsevier.com/locate/pss

# Ganymede's internal structure including thermodynamics of magnesium sulfate oceans in contact with ice

Steve Vance [a,b,*], Mathieu Bouffard [c], Mathieu Choukroun [a,b], Christophe Sotin [a,b]

[a] Jet Propulsion Laboratory, Caltech, 4800 Oak Grove Drive, Pasadena, CA 91109, USA
[b] NASA Astrobiology Institute, Icy Worlds Team, USA
[c] Ecole Normale Supérieure de Lyon, France

ARTICLE INFO

*Article history:*
Received 29 June 2013
Received in revised form
8 March 2014
Accepted 12 March 2014
Available online 12 April 2014

*Keywords:*
Ganymede
High pressure
Oceanography
Equations of state
JUICE
Geophysics

ABSTRACT

The large icy moons of Jupiter contain vast quantities of liquid water, a key ingredient for life. Ganymede and Callisto are weaker candidates for habitability than Europa, in part because of the model-based assumption that high-pressure ice layers cover their seafloors and prevent significant water–rock interaction. Water–rock interactions may occur, however, if heating at the rock–ice interface melts the high pressure ice. Highly saline fluids would be gravitationally stable, and might accumulate under the ice due to upward migration, refreezing, and fractionation of salt from less concentrated liquids. To assess the influence of salinity on Ganymede's internal structure, we use available phase-equilibrium data to calculate activity coefficients and predict the freezing of water ice in the presence of aqueous magnesium sulfate. We couple this new equation of state with thermal profiles in Ganymede's interior—employing recently published thermodynamic data for the aqueous phase—to estimate the thicknesses of layers of ice I, III, V, and VI. We compute core and silicate mantle radii consistent with available constraints on Ganymede's mass and gravitational moment of inertia. Mantle radii range from 800 to 900 km for the values of salt and heat flux considered here (4–44 mW $m^{-2}$ and 0 to 10 wt% $MgSO_4$). Ocean concentrations with salinity higher than 10 wt% have little high pressure ice. Even in a Ganymede ocean that is mostly liquid, achieving such high ocean salinity is permissible for the range of likely S/Si ratios. However, elevated salinity requires a smaller silicate mantle radius to satisfy mass and moment-of-inertia constraints, so ice VI is always present in Ganymede's ocean. For lower values of heat flux, oceans with salinity as low as 3 wt% can co-exist with ice III. Available experimental data indicate that ice phases III and VI become buoyant for salinity higher than 5 wt% and 10 wt%, respectively. Similar behavior probably occurs for ice V at salinities higher than 10 wt%. Flotation can occur over tens of kilometers of depth, indicating the possibility for upward 'snow' or other exotic modes of heat and material transport.



## 1. Introduction

Ganymede and Europa are fully differentiated planetary bodies, as indicated by measurements of gravitational moments of inertia (Anderson et al., 2004; Sotin and Tobie, 2004). Internal heating in these bodies comes from radiogenic and tidal heating due to a resonant forced eccentricity in their orbits around Jupiter. Composition and heat flux assessments for Europa and Ganymede lead to the prediction of liquid oceans, a presumed prerequisite for life. These predictions are supported by induced magnetic field measurements at Europa and Callisto (Khurana et al., 1998; Kivelson et al., 2002) and plausibly also for Ganymede. The internally generated magnetic field in Ganymede's metallic core complicates interpretation of an induced field from Jupiter (Kivelson et al., 2002), but the internal dynamo and surface that is geologically younger than Callisto's indicate that Ganymede is warm enough to support an ocean. Intrinsic to these measurements is an assertion that the oceans are electrically conductive and therefore saline.

The configurations of liquid and solid $H_2O$ layers in the icy Galilean satellites are dictated by interior heat flux, the composition of dissolved constituents, and their influence on pressure- and temperature-dependent freezing points and specific densities. Temperatures range from approximately 100 K on average at the surfaces of both bodies, to nearly 280 K in high-pressure ice VI at the bottom of Ganymede's $H_2O$ layer.

* Corresponding author at: Jet Propulsion Laboratory, Caltech, 4800 Oak Grove Drive, Pasadena, CA 91109, USA. Tel.: +1 626 437 6200.
*E-mail address:* svance@jpl.nasa.gov (S. Vance).

http://dx.doi.org/10.1016/j.pss.2014.03.011
0032-0633/

Europa's internal structure is consistent with a liquid ocean in direct contact with rock—a necessary condition for water–rock interactions that may be essential for life's origin (Martin et al., 2008). Hydrostatic pressures approach 200 MPa at Europa's seafloor, only slightly above those at the deepest part of Earth's ocean, where organisms persist (Yayanos, 2001). Ganymede's larger size and higher abundance of water relative to denser mantle materials create pressures as high 1.2 GPa at the water–rock interface. Under these conditions it is expected that any liquid ocean in its interior will be sandwiched between layers of ice I and ice V and VI, with the thermodynamic and rheological properties of these layers determining the efficiency of heat transport from the water–rock interface into the overlying ocean (Sotin and Tobie, 2004).

The influence of salinity on Ganymede's ice layer thickness has not been thoroughly assessed [but see Grindrod et al., 2008, for related efforts]. We compile available phase data for freezing in this system to construct an equilibrium model for freezing of relevant ice phases. We apply this new tool to estimating the thicknesses of Ganymede's ocean, various ice phases, silicate mantle, and iron core. We consider a range of bulk ocean compositions and heat flux values. Central to these calculations is the use of newly available thermodynamic data for aqueous $MgSO_4$ (Vance and Brown, 2013) and the development of an activity model for the equilibrium of water ice phases in the presence of salt. We apply these results in the context of existing constraints on Ganymede's mass and gravitational moment of inertia. In the discussion section we explore the dynamical stability of ice and liquid layers.

## 2. Compositions of oceans in the Galilean satellites

Icy satellite ocean compositions have been broadly assumed to be dominated by $MgSO_4$ on the basis of equilibrium chemical models of bulk water–rock interactions in their interiors [e.g., Zolotov and Kargel, 2009]; the expectation is plausibly confirmed by infrared absorption spectra in the 2.5 μm spectral region by the Near-Infrared Mapping Spectrometer on the Galileo mission [e.g., Carlson et al., 2009; Dalton et al., 2012]. Primordial water–rock interactions in CI or CL chondrite parent accreting materials would be expected to extract fluids dominated by dissolved $Na^+$ and $Cl^-$, but high bulk water–rock ratios relative to Earth and the loss of hydrogen to space and attendant lowering of hydrogen fugacity $fH_2$ would favor a rise in the solubility of sulfate and $Mg^{+2}$ (Zolotov and Kargel, 2009).

Several exceptions may be raised to the conventional story of icy satellite ocean composition. Recent ground-based observations by Brown and Hand (2013) were interpreted as indicating magnesium sulfate forms predominantly on Europa's more irradiated trailing hemisphere. They conclude that sulfur on Europa's surface is imported from Io, and magnesium deposited on Europa's surface from below arrives in the form of $MgCl_2$. If true, Europa's ocean may be relatively alkaline or may have a low effective water–rock ratio. Europa is smaller than Ganymede, suggesting greater ease of losing hydrogen. It is also more strongly tidally heated, consistent with a high degree of water–rock interaction. Vance et al. (2007) note that very high pressures at the water–rock interfaces in large ocean planets like Ganymede would tend to close microfractures and prevent significant water rock interaction after differentiation. In very large icy satellites like Ganymede, then, high water–rock ratio and high seafloor pressure might suggest an ability to retain materials extracted from the rocky interior during differentiation. We assume that these materials are predominantly $MgSO_4$ while pointing out that the phenomena we describe are also likely to occur, to differing degrees, for other ocean compositions [e.g., Journaux et al., 2013].

We estimate the maximum allowed ocean salinity of $MgSO_4$ by considering the partitioning of sulfur between Ganymede's core and ocean. The molten portion of Ganymede's core—a requirement for generating its intrinsic magnetic field (Kivelson et al., 2002)—probably has an Fe–FeS eutectic composition (Poirier, 1994). In the context of modeling Ganymede's dynamo, Hauck et al. (2006) treat a wide range of sulfur for Ganymede's core, whereas Bland et al. (2008) suggest that the sulfur content must be either very low ($<3$ wt%) or very high ($>21$ wt%). As a conservative estimate of sulfur partitioning between Ganymede's ocean and core, we consider a eutectic core composition of 25 wt% S, between the eutectic concentration at 1 and 10 GPa as measured by Fei et al. (1997).

The molten core that generates Ganymede's intrinsic magnetic field is probably small, as indicated by the small quadrupole coefficients measured by the Galileo magnetometer. Kivelson et al. (2002) constrain the liquid core radius to 130 km by applying an approach used for the Earth and other planets. They note that the result may be misleading, however, because the Earth's quadrupole power is lower by almost an order of magnitude than the trend provided by the dipole moment and the $n>2$ multipole moments. A more reliable determination of the core radius from multipole components awaits measurements by the European Space Agency's JUpiter ICy moon Explorer (JUICE) mission (Grasset et al., 2013).

Measurements of the position dependent gravitational field through spacecraft Doppler radio tracking provide additional insight into coupled core size and density. The solution given by the gravity data is non-unique, but Anderson et al. (2004) propose that the iron core has a radius between 650 and 1300 km. Gravity constraints forbid the core radius from exceeding half of the moon's radius ($\sim$1300 km). In our models we assess self-consistent densities, depths, and compositions of core and mantle that result from detailed assessments of the ocean and ice structure that account for ocean salinity, using $MgSO_4$ as a representative composition for which good chemical data are available. Models that do not include a metallic core require a high bulk silicate density exceeding 3600 kg $m^{-3}$, indicating the absence of hydrated materials. For a representative mantle density of 3250 kg $m^{-3}$, consistent with the presence of modest amounts of hydrated materials, we arrive at interior structures comparable to those obtained by previous investigators.

## 3. Activity model for ices in the presence of $MgSO_4$

Provided accurate data are available, the chemical potential $\mu_{H_2O}(P,T)$ for a given phase can be obtained from the thermodynamic expression:

$$\mu_{H_2O}(P,T) = H^o(P_o,T_o) + \int_{T_o}^{T} C_P\, dT' - T\left(S^o(P_o,T_o) + \int_{T_o}^{T} \frac{C_P}{T'}\, dT'\right) + \int_{P_o}^{P} V(P',T)\, dP' \quad (1)$$

where $H^o(P_o,T_o)$ and $S^o(P_o,T_o)$ are, respectively, the enthalpy and entropy at reference standard laboratory conditions of pressure and temperature $(P_o,T_o)$, $C_P$ is the heat capacity, and $V$ corresponds to the specific volume (primes denote variables of integration). Phase equilibrium is defined for a given salt concentration by the pressure and temperature where solid ($S$) and liquid ($L$) potentials are equal, $\mu^L=\mu^S$. We adopt the thermodynamic representation of Choukroun and Grasset (2010) for solid phases of pure water, and develop a representation for the activity of the liquid phase (aqueous $MgSO_4$) using the same Margules framework for non-ideal solutions (Grover, 1977) that they previously applied to the ammonia water system. We construct activity coefficients over the

m-P-T range of interest using least squares fitting of experimental phase equilibrium data for the pure water ice phase boundary in the presence of dissolved magnesium sulfate.

We calculate the chemical potential of aqueous $MgSO_4$ using the general formulation for a non-ideal solution

$$\mu^L_{H_2O}(P,T,X^L_{H_2O}) = \mu^L_{H_2O}(P,T,1) + RT\ln(\gamma^L_{H_2O}X^L_{H_2O}) \quad (2)$$

where $\gamma^L_{H_2O}$ is the activity coefficient of water in the liquid phase and $X^L_{H_2O}$ the molar fraction of water in this phase.

To describe the phase behavior, we use a formulation based on the Margules equations, in which the activity coefficient is expressed as

$$RT\ln\gamma^L_{H_2O} = W(1-X^L_{H_2O})^2 \quad (3)$$

The formulation for the Margules coefficient $W$ adopted here depends on both temperature and pressure:

$$W = w_0(1+w_1\tanh(w_2P))\left(1+\frac{w_3}{(T-T_o)^2}\right), \quad (4)$$

with $w_0 = -1.8\times10^6$ J mol$^{-1}$, $w_1 = 150$, $w_2 = 1.45\times10^{-4}$ MPa$^{-1}$, $w_3 = -12$ K$^2$ and $T_o = 246$ K. The resulting coefficients reproduce available data, allowing us to construct a phase diagram for pure ice in the presence of dissolved magnesium sulfate up to the pressure- and temperature-dependent eutectic composition (Fig. 1).

Available experimental phase data for the pure water ice phase boundary in the presence of dissolved magnesium sulfate are employed as follows: Fortes and Choukroun (2010), covering the liquidus with Ice Ih at atmospheric pressure; Hogenboom et al. (1995), covering the liquidus with Ice V at $P = 390$ MPa (Fig. 2a). We also use eutectic melting curve (composition of the lowest melting temperature) pressure dependence, reported as temperature and pressure coordinates (Fig. 2b) or as composition and pressure (Fig. 3). We do not consider eutectic solutions in the present application of our activity model to Ganymede's interior, but the model is appropriate for such applications. Most of the eutectic data come from Hogenboom et al. (1995). For $P > 390$ MPa, we adopt a polynomial fit between the experimental melting points of Nakamura and Ohtani (2011) at pressures near 2 GPa and eutectic data at 390 MPa from Hogenboom et al. (1995) (Fig. 2), with additional data from Grasset et al., 2001 in the range from 0 to 600 MPa.

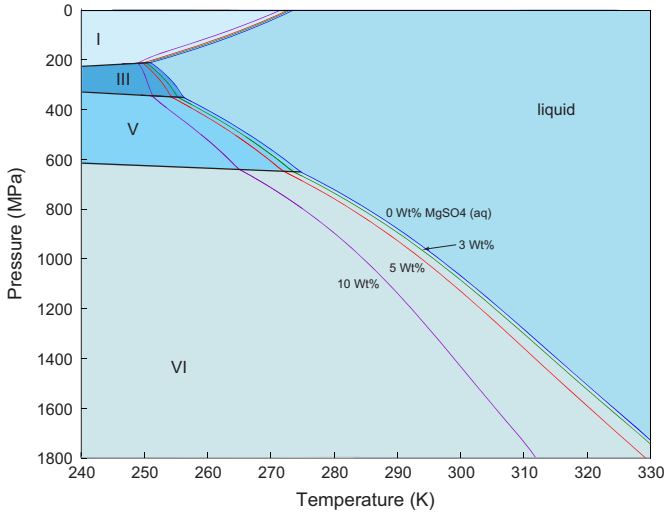


**Fig. 1.** Water ice phase stability in the presence of $MgSO_4$ (aq) in concentrations of {0, 3, 5, 10} wt% as a function of pressure, in MPa, on the vertical axis (increasing downward), and temperature, in K, on the horizontal. Increasing concentration decreases the temperature of freezing at a given pressure for all phases, and decreases the pressure of freezing at constant temperature for ice I while increasing it for the other phases.

The transition in slope of the eutectic curves shown in Fig. 2 probably arises from the transition between hydration states of precipitated magnesium sulfate $MgSO_4\cdot x\ H_2O$, from the more hydrated ($x=11$) phase at lower pressures to the denser and less hydrated phase ($x=7$) above 1.8 GPa, as discussed by Fortes et al. (2008). Understanding the transition gives us confidence in the downward trend of the two data points from Nakamura and Ohtani (2011). We regard those results with some skepticism because the experimental design, as described, did not wait for thermodynamic equilibrium to be achieved, implying an inaccuracy due to supercooling that might be larger than indicated by our assessed error bars.

We discuss possible implications of the activity model for our model results for the ganymede ocean with 10 wt% $MgSO_4$ (aq) in Section 5. Further experimental work would be helpful to clarify the eutectic melting curve between 600 MPa and 2 GPa.

## 4. Application to Ganymede

To assess the effect of dissolved $MgSO_4$ on the melting of water ices in Ganymede using our equations of state, we construct thermal profiles consistent with the expected range of internal heat fluxes from Ganymede's interior, past and present (Section 4.1), and we describe interior structures that comply with prior knowledge of mass and moment of inertia (Section 4.2).

### 4.1. Thermal profiles

We assume a surface temperature $T_o = 110$ K, the average surface temperature of Ganymede (McFadden et al., 2007). Thermal profiles are determined using an iterative method. At each step of depth, the new pressure, temperature, ice–liquid equilibrium state, and associated thermodynamic properties are calculated using the values found at the preceding step. The calculation for Ganymede's uppermost ice I layer is divided by 20 steps, and the remaining region below is divided into 500 steps. In each step we calculate the gravitational acceleration from the mass of the underlying material. Gravitational acceleration increases with depth in the ice and liquid layers because their density is much lower than that of silicates and iron. The variation can be as large as 25% of the value at the surface ($g_o = 1.4$ m s$^{-2}$). For this reason, we calculate the adiabatic gradient in the liquid layer as a function of pressure.

Computing fluid behaviors to pressures at the silicate interface requires that we extrapolate the thermodynamic calculation to 1.5 GPa. This is well beyond the 800 MPa limit recommended by Vance and Brown (2013), but the extrapolation is smooth in all thermodynamic properties for concentrations up to the 10 wt%. Examining the effects of higher concentrations requires obtaining thermodynamic data for $MgSO_4$ solutions at diamond-anvil-cell pressures.

The conductive temperature profile for the ice I upper layer assumes temperature-dependent conductivity of the form $k = D/T$, the temperature profile may be represented as a function of depth $z$ as

$$T(z) = T_b^{z/z_b}\,T_o^{1-z/z_b}, \quad (5)$$

with corresponding heat flux at the ice I–water interface ($z_b$ and $T_b$)

$$q_b = D\frac{\ln T_b/T_s}{z_b}. \quad (6)$$

Using $D = 632$ W m$^{-1}$ (Andersson and Inaba, 2005) provides an accuracy of better than 10% in the range of temperatures from 100

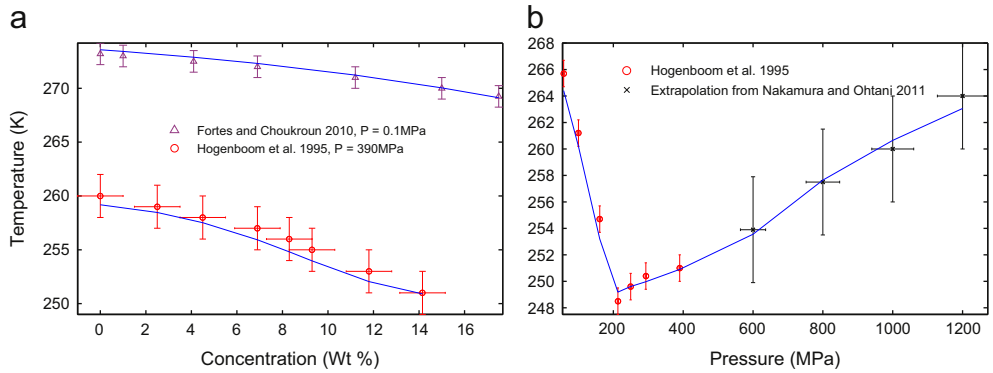


**Fig. 2.** Interpolation of experimental solidus and eutectic temperatures, respectively, for aqueous $MgSO_4$ versus concentration (a) and pressure (b). Predictions based on the Margules activity model presented here (solid lines) fit reference values within the range of the assessed experimental errors shown. Absolute misfits are less than 0.5%.

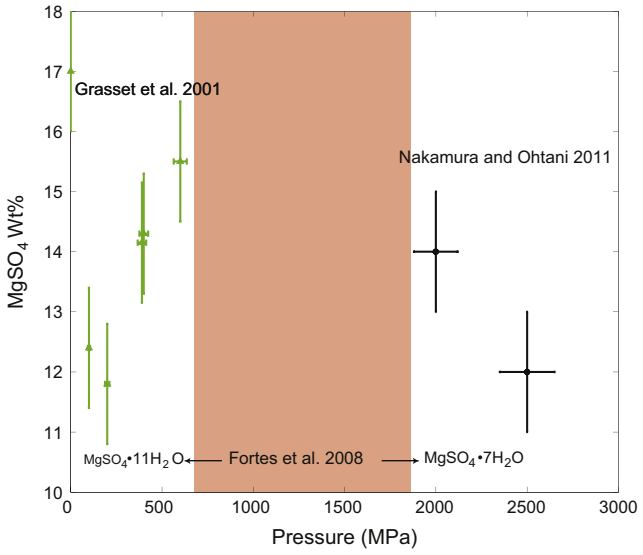


**Fig. 3.** Available measurements of eutectic composition for $MgSO_4$ (aq) as a function of pressure, with assessed uncertainties. Measurements for $P < 600$ MPa by Grasset et al., 2001 show how the eutectic composition decreases with pressure below 300 MPa, then increases again at higher pressures. Higher-pressure measurements by Nakamura and Ohtani (2011) show that the eutectic decreases again at pressures unlikely to occur in Ganymede's ocean. The shaded region spanning 600–1800 MPa corresponds to the transition in precipitated $MgSO_4 \cdot xH_2O$ from $x=7$ to 11 (Fortes et al., 2008), which plausibly explains the change from positive to negative slope.

to 270 K. The approach is similar to that used by McKinnon (2006) for investigating Callisto's icy lithosphere. Other thermodynamic properties for water ice are taken from Choukroun and Grasset (2010). Temperature values between 250 and 270 K chosen for the lower boundary condition $T_b$ correspond to the liquidus with ice I over the range of eutectic temperatures for the (aq) $MgSO_4$ sulfate system. Equivalent equilibrium heat flow values calculated from Eq. (6) are 4–44 mW $m^{-2}$, in the range anticipated for present-day radiogenic heating alone to one more consistent with estimates that include tidal heating [7120 mW $m^2$; Bland et al., 2009]. Representative values for heat flux and ice layer thicknesses are included in Table 2.

The liquid ocean is assumed to be unstratified for simplicity, with a convective adiabatic thermal profile

$$\frac{dT}{dP} = \frac{\alpha T}{\rho C_P} \tag{7}$$

in which $\alpha$ is the thermal expansivity of the fluid. Fluid properties $\alpha$, $C_P$ and $\rho$ are calculated from the thermodynamic data obtained by Vance and Brown (2013). At lower pressures for salty oceans, $\alpha$ approaches zero and even becomes negative near the freezing point of the fluid. Consequently, the upper portion of the ocean may become weakly convecting or stratified, as explored in the context of Europa's ocean by Melosh et al. (2004), Vance and Brown (2005), Vance and Goodman, 2009. A non-convecting ocean should accumulate heat and subsequently reinitiate convection, though more exotic behavior may occur where boundaries between ice I and ice III merge (Kirk and Stevenson, 1987). We assume that our model ocean convects even for the few cases where $\alpha$ is slightly negative, because the resulting profile is essentially isothermal in the few km of ocean where $\alpha < 0$.

Table 1 shows the range of variation in fluid thermodynamic properties encountered in our model of Ganymede's ocean. The values serve as a basis for comparison simplifying thermodynamic assumptions employed in previous work [e.g., Showman et al., 1997], and as a reference for those wishing to reproduce our results. Values are also given at 0.1 MPa and 273.15 K for comparison with conditions more commonly found on Earth. The table includes values for $\rho$, $\alpha$, and $C_P$ for the top and bottom of the ocean, calculated for {0,3,5,10} wt% solutions at the lowest and highest bottom melting temperature, along with corresponding depths, pressures, and temperatures. The ratio $\alpha/\rho C_P$ increases by as much as a factor of three between the top and bottom of the ocean.

Densities of high pressure ice phases come from the state equations of Choukroun and Grasset (2010). Monoclinic ice V has a less compact structure than the higher-pressure tetragonal polymorph ice VI, and is therefore less dense. As discussed in Section 5, ice III, also tetragonal but of much lower density, can form at low temperatures created by even moderately saline ocean compositions, but becomes convectively unstable at salinity greater than 5 wt% at depths where it forms.

For monotonic cooling of the deep interior in a differentiated world with a deep ocean, high pressure ices should only form when the heat flux from the interior becomes low enough to support their formation. However, as pointed out for Titan by Tobie et al. (2005), "The early thermal evolution of a homogeneous chondritic core is characterized by a temperature increase controlled by diffusive heating, followed by marginal convection about 1 Ga after core overturn." Owing to this, we assume that the high pressure ices form early in Ganymede's history but dissipate mantle heat inefficiently. We do not account for convection in high pressure ices, but approximate two-phase flow [e.g., Šrámek et al., 2007] by setting the geothermal profile to follow the liquidus line, as proposed by Cassen et al. (1980). This provides a density profile that is approximately correct for the purpose of determining Ganymede's internal structure from measured mass and moment of inertia. Our model assumes that the bottom

**Table 1**
Thermodynamic properties of fluids in Ganymede oceans: pressure $P$, temperature $T$, liquid thermal expansivity $\alpha$, specific heat capacity $C_P$, and density $\rho$. For each ocean salinity $w$, in the range {0, 3, 5, 10} wt%, equivalent depths $z$ are provided, along with fluid properties at the ice I–ocean interface (unshaded) and high-pressure ice interfaces that constitute the seafloor (lightly shaded lines). Two sets of unshaded and lightly shaded lines are given for each ocean composition: one for the lowest value of ice Ih melting temperature considered, which decreases as ocean salinity increases, and one for the highest value of 270 K. The ratio $\alpha/\rho C_P$ varies substantially between the ocean's top and bottom. Darkly shaded rows for each ocean composition provide reference thermodynamic values at 0.1 MPa at the 273.15 K freezing point of pure water.

| $w$ (wt%) | $z$ (km) | $P$ (MPa) | $T$ (K) | $\alpha$ ($10^{-4}$ K$^{-1}$) | $C_P$ ($10^3$ J/kg/K) | $\rho$ ($10^3$ kg m$^{-3}$) | $\frac{\alpha}{\rho C_P}$ ($10^{-11}$ Pa$^{-1}$) |
|---|---|---|---|---|---|---|---|
| 0 | – | 0.1 | 273.15 | −0.68 | 4.22 | 1.00 | −1.60 |
| | 134 | 181 | **255.0** | 1.34 | 3.34 | 1.08 | 3.71 |
| | 252 | 378 | 258.3 | 2.59 | 2.77 | 1.14 | 8.21 |
| | 32 | 42 | **270.0** | 0.34 | 4.04 | 1.02 | 0.83 |
| | 538 | 915 | 292.6 | 4.62 | 3.80 | 1.23 | 9.90 |
| 3 | – | 0.1 | 273.15 | 0.002 | 4.07 | 1.03 | 0.04 |
| | 144 | 195 | **252.5** | 0.45 | 2.86 | 1.11 | 1.42 |
| | 189 | 271 | 253.0 | 0.97 | 2.57 | 1.14 | 3.33 |
| | 27 | 36 | **270.0** | 0.62 | 3.91 | 1.05 | 1.50 |
| | 541 | 939 | 292.6 | 4.15 | 3.43 | 1.26 | 9.61 |
| 5 | – | 0.1 | 273.15 | −0.38 | 3.96 | 1.05 | 0.91 |
| | 141 | 191 | **252.5** | 0.18 | 2.72 | 1.13 | 0.57 |
| | 205 | 299 | 253.0 | 0.73 | 2.32 | 1.16 | 2.70 |
| | 24 | 31 | **270.0** | 0.74 | 3.81 | 1.07 | 1.82 |
| | 561 | 992 | 293.5 | 3.93 | 3.32 | 1.28 | 9.24 |
| 10 | – | 0.1 | 273.15 | 1.17 | 3.67 | 1.11 | 2.88 |
| | 148 | 200 | **250.0** | −0.32 | 2.24 | 1.18 | −1.20 |
| | 178 | 254 | 250.0 | 0.00 | 2.05 | 1.20 | 0.00 |
| | 13 | 17 | **270.0** | 1.07 | 3.55 | 1.12 | 2.70 |
| | 766 | 1469 | 301.2 | 2.37 | 2.84 | 1.38 | 6.05 |

temperature increases until it reaches the melting temperature of ice VI at the rock–ice VI interface. Formation of liquid triggers instabilities: dilute solutions ($\lesssim$5 wt% for Ganymede) are less dense than ices V and VI (Fig. 4). Liquid diapirs may freeze before reaching the top boundary, precipitating salt as they do. Precipitated salts, and any rocky material falling through the overlying ice I and ocean, will be denser than high pressure ice phases, and should sink toward the rock–ice interface. Brines have intermediate densities that often exceed those of high pressure ices, and should also tend to move downward through the ice.

Heat flux at the upper ice VI boundary should exceed that at the ice VI–rock interface because of tidal dissipation. The amount of tidal dissipation depends on the viscosity of ice VI at its melting point. Laboratory experiments suggest values of $10^{14}$ Pa s (Poirier et al., 1981) would lead to significant tidal heating, but the high deviatoric stresses used in laboratory experiments may not extrapolate predictably to the low stress field expected in the ice VI layer. Even small amounts of tidal heating, combined with the low thermal conductivity, suggest that the high pressure ice should be everywhere at its melting temperature.

### 4.2. Interior models

We use the equation of state of $MgSO_4$ to calculate density and temperature profiles in the ocean in a 1-D spherical model. The equations of state of the different phases of ice determine the density profiles in the different icy layers as described above. Since the total mass ($M$) and the moment of inertia ($C$) of Ganymede are known, we use that information to constrain the density profile in the core. The model includes a liquid iron core to explain the observation of a deep intrinsic magnetic field (Kivelson et al., 2002). Four parameters are unknown: the densities and radii of the silicate layer and of the iron core ($\rho_{sil}$, $\rho_{iron}$, $R_{sil}$, $R_{iron}$). As described below, the two densities are prescribed and the two radii are determined from the knowledge of mass and moment of inertia.

The total mass can be calculated as the sum of nested spherical shells of radius $r$ having an infinite small thickness $dr$ with constant density $\rho(r)$:

$$M = \int_M dm = 4\pi \int_{R_{sil}}^{R} \rho(r) r^2\, dr + \frac{4\pi}{3}\rho_{sil} R_{sil}^3 = M_{H_2O} + \frac{4\pi}{3}\rho_{sil} R_{sil}^3 \quad (8)$$

where the $M_{H_2O}$ includes the mass of the low-pressure ice upper layer, the ocean, and the high-pressure ice layers. The moment of inertia can be written as

$$C = \int_M x^2\, dm = \int\int\int r^4 \rho(r,\theta,\psi)\, \sin^3(\theta)\, dr\, d\theta\, d\psi = \frac{8\pi}{3}\int_{R_{sil}}^{R} \rho(r) r^4\, dr + \frac{8\pi}{15}\rho_{sil} R_{sil}^5 = C_{H_2O} + \frac{8\pi}{15}\rho_{sil} R_{sil}^5 \quad (9)$$

where $x$ is the distance of any element of mass ($dm$) to the spin axis. Starting from the surface ($R_{sil} = R - dr$), the radius of the silicate interface is decreased by $dr$. We calculate the value of the upper layer mass ($M_{H_2O}$) and moment of inertia ($C_{H_2O}$) with each step. The value of the radius of the interface ($R_{sil}$) gives the silicate density from Eq. (8). We use this value to calculate the moment of inertia from Eq. (9) for different values of the temperature at the base of the ice I layer and for different amounts of $MgSO_4$ in the ocean.

To include an iron core layer, we must prescribe two of the four parameters: the radius of the silicate–ice interface ($R_{sil}$), the radius of the iron core ($R_{iron}$), the density of the silicates ($\rho_{sil}$) and the density of the iron core ($\rho_{core}$). We choose to prescribe the densities because they can be investigated for a range of reasonable values.

Since there is an iron core, we assume that silicates are dehydrated and that the density of the silicates is lower than 3500 kg m$^{-3}$ because a lot of iron has migrated to form the iron-rich core. Therefore, the nominal case is a silicate mantle with a density of 3250 kg m$^{-3}$. Following Bland et al. (2008), the density of the iron core can vary between that of pure iron ($\rho_{iron}$=8000 kg m$^{-3}$) and that of pure FeS ($\rho_{iron}$=5150 kg m$^{-3}$).

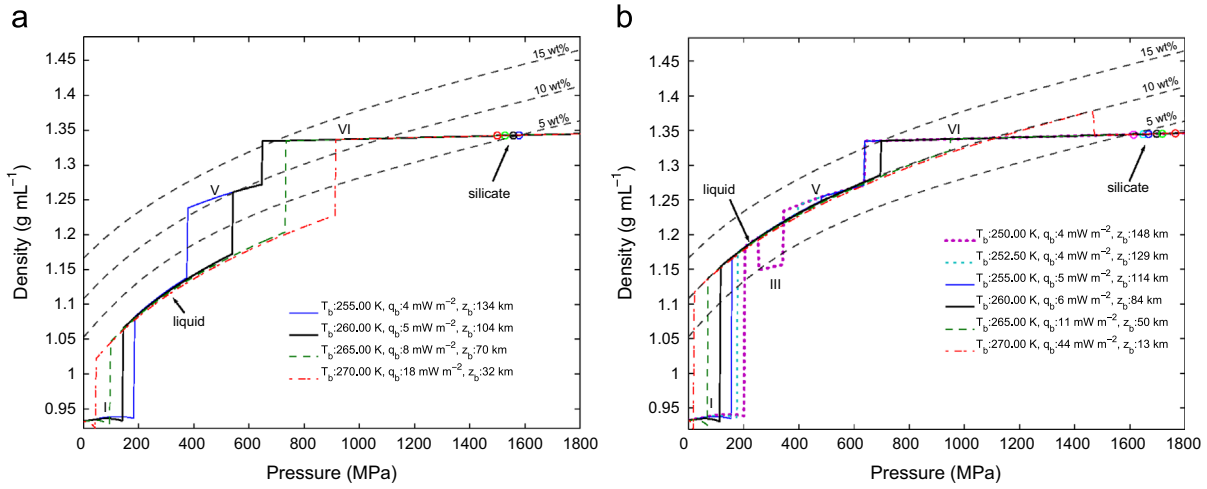


**Fig. 4.** Density profiles in Ganymede's interior for Ice I melting temperatures $T_b$ between 250 K and 270 K for a uniform ocean $MgSO_4$ salinity of 0 wt% (a) and 10 wt% (b). Dashed lines denote the density of aqueous $MgSO_4$–$H_2O$ along the liquidus lines with ices for concentrations of {5,10,15} wt%, increasing upward in concentration. Circles indicate the computed pressure at the silicate mantle consistent with Ganymede's mass and moment of inertia. Dashed lines denote the density of aqueous $MgSO_4$–$H_2O$ along the liquidus lines with ices for concentrations of {5,10,15} wt%, increasing upward in concentration. Ice III is thermodynamically stable for the 10 wt% case with $T_b$=250 K, but is less dense than the ocean fluid. Flotation is similarly expected for ice V at slightly higher ocean concentrations. Ice VI is likewise less dense than the fluids at the seafloor for $T_b$=270 K. Flotation occurs for a substantial part of the stability field, corresponding to tens of kilometers of depth. $R_{sil}$ increases with $T_b$ for the 0 wt% case but decreases for the 10 wt% case.

The nominal model uses the eutectic value for the density of the iron core, where FeS ($X_{FeS}$) is 25%

$$\rho_{iron} = \frac{\rho_{Fe}\rho_{FeS}}{X_{FeS}(\rho_{Fe}-\rho_{FeS})+\rho_{FeS}} = 7030 \text{ kg m}^{-3}. \quad (10)$$

Based on these assumptions we determine the moment of inertia numerically from

$$M_{iron} = M - M_{H_2O} - \frac{4\pi}{3}\rho_{sil}(R_{sil}^3 - R_{iron}^3) \quad (11)$$

$$R_{iron} = \left( \frac{M - M_{H_2O} - \frac{4\pi}{3}\rho_{sil}R_{sil}^3}{\frac{4\pi}{3}(\rho_{iron}-\rho_{sil})} \right)^{1/3} \quad (12)$$

$$C = C_{H_2O} + \frac{8\pi}{15}(\rho_{sil}(R_{sil}^5 - R_{iron}^5) + \rho_{iron}R_{iron}^5) \quad (13)$$

Resulting values, listed in Table 2 and displayed in Figs. 4 and 5, are within the 1% error of the available constraints on moment of inertia. Corresponding uncertainty in the core and mantle radii ($R_{core}$ and $R_{sil}$) are $\pm$65 km and $\pm$20 km, respectively.

## 5. Results and discussion

Density profiles for uniform ocean concentrations of 0 and 10 wt%, up to the nominal 1200 MPa pressure at Ganymede's water rock interface, are displayed in Fig. 4 for $T_b$ between 250 and 270 K. Corresponding depths and geothermal profiles in Fig. 5 illustrate relative thicknesses of various layers (also see Table 2). Circles and horizontal lines, used respectively in the two sets of figures, indicate the pressure and depths at the silicate mantle interface with ice VI. Mass and moment-of-inertia constraints require that $R_{sil}$ decrease with increasing $T_b$ for the 0 wt% ocean and increase for the 10 wt% case. Transitions from ice I to liquid, and to ice III, V, and VI, show as discontinuities in density as pressure increases. Adiabatic profiles for oceans containing $MgSO_4$ in concentrations of {5, 10, 15} wt% (dashed lines) illustrate how fluid densities exceed those of surrounding high pressure ice phases for concentrations higher than 10 wt%. A profile for $T_b$=250 K reveals the presence of a thin layer of liquid above 200 MPa in the presence of ice III. In our models, thermally conducting ice I layer ranges in thickness from 144 km (3 wt% ocean with $T_b$=252.5 K) to 13 km (10 wt% ocean with $T_b$=270 K; see Table 2). Corresponding heat flux values (Eq. (6)) range from 4 mW m$^{-2}$ to 44 mW m$^{-2}$. The upper range is inconsistent with the suppressed freezing point at elevated salt concentration, and requires tidal heating (Bland et al., 2009). Insulation of the ice shell by dust and other non-icy materials may allow for a thinner ice shell with less heat flux, but the melting temperature is not consistent with the high salt composition unless the ocean is compositionally stratified. Such scenarios are beyond the level of complexity considered here.

Depending on the efficiency of transporting liquid through high-pressure ice, material from a brine pocket in contact with Ganymede's mantle might reach the upper ocean and deliver chemical compounds extracted from the mantle (Barr et al., 1781). Alternatively, if the majority of upwelling liquid plumes refreeze into the ice VI layer, fractionation of liquids would lead to a poorly defined amount of incorporation of salts into the ice structure (Journaux et al., 2013), with remaining negatively buoyant fluids migrating downward and thereby enriching the salt content of fluids at the water–rock interface. A stable liquid layer might evolve in this way, with salt composition exceeding about 5 wt%.

We do not expect liquids to form below high pressure ice layers for a homogeneous Ganymede that has cooled throughout its history [as treated by Kirk and Stevenson, 1987]. Secular variations in Ganymede's orbit and obliquity almost guarantee oscillations in tidal heat input (Hussmann and Spohn, 2004), and it is also possible that radiogenic heat from interior was initially small (Schubert et al., 2010). Similarly, the global pattern of heat dissipation will vary based on heat escaping from the core (e.g., the locations of hot spots) and the manner of ocean circulation [e.g., whether zonal jets and Coriolis confined plumes occur; Vance and Goodman, 2009; Travis et al., 2012; Soderlund et al., 2014].

The thickness of the high pressure phases of ice between the ocean and the silicate layer decreases with increasing values of the heat flux because $\alpha/\rho C_P$ increases with pressure (Table 1), while also decreasing with increasing salinity. The decrease is partly balanced by the lower value of the radius of the silicate–ice interface as the density of the ocean increases with salinity. It is also worth noting that a higher value of the moment of inertia

**Table 2**
Model results for Ganymede for ocean salinities of {0, 3, 5, 10} wt% $MgSO_4$(aq) for bottom melting temperatures of the ice Ih layer ($T_b$) from 250 to 270 K. Zero values of thickness indicate that the phase is not present for the given composition and bottom melting temperature. Columns with dashes indicate conditions for which salinity is too low to permit the presence of liquid. Ice and ocean layer thicknesses (in km) are shown in the unshaded lines. The top line for each ocean concentration provides heat flux $q_b$ (in mW $m^{-2}$; Eq. (6)) for the thermal profile Eq. (5) that corresponds to the equilibrium ice Ih thickness. Shaded lines in the lower region for each composition indicate mantle and core radii in the lower portion, calculated as described in Section 4.2, consistent with observed moment of inertia of $C/MR^2 = 0.3105 \pm 0.0028$. The 1% error in moment of inertia corresponds to uncertainty in the mantle and core radii of about $\pm 20$ km and $\pm 65$ km, respectively, for all of the above cases. The last line for each ocean concentration provides the S/Si mass fraction for Ganymede consistent with the interior structure (also shown in Fig. 6).

| wt% | | K | | | | | |
|---|---|---|---|---|---|---|---|
| | | 250 | 252.5 | 255 | 260 | 265 | 270 |
| 0 | $q_b$ | – | – | 4 | 5 | 8 | 18 |
| | Ice Ih | – | – | 134 | 104 | 70 | 32 |
| | Liquid | – | – | 119 | 239 | 375 | 506 |
| | Ice III | – | – | 0 | 0 | 0 | 0 |
| | Ice V | – | – | 142 | 55 | 0 | 0 |
| | Ice VI | – | – | 426 | 416 | 360 | 260 |
| | $R_{mantle}$ | – | – | 1814 | 1820 | 1829 | 1836 |
| | $R_{core}$ | – | – | 690 | 680 | 667 | 658 |
| | S/Si | – | – | 4.60 | 4.42 | 4.37 | 4.26 |
| 3 | $q_b$ | – | 4 | 4 | 5 | 8 | 21 |
| | Ice Ih | – | 144 | 130 | 100 | 66 | 27 |
| | Liquid | – | 45 | 121 | 233 | 372 | 514 |
| | Ice III | – | 46 | 0 | 0 | 0 | 0 |
| | Ice V | – | 157 | 139 | 60 | 0 | 0 |
| | Ice VI | – | 434 | 438 | 434 | 387 | 282 |
| | $R_{mantle}$ | – | 1807 | 1806 | 1807 | 1809 | 1811 |
| | $R_{core}$ | – | 703 | 702 | 699 | 701 | 700 |
| | S/Si | – | 5.04 | 5.51 | 6.03 | 6.77 | 7.52 |
| 5 | $q_b$ | – | 4 | 4 | 6 | 9 | 24 |
| | Ice Ih | – | 141 | 127 | 96 | 63 | 24 |
| | Liquid | – | 64 | 128 | 243 | 381 | 537 |
| | Ice III | – | 29 | 0 | 0 | 0 | 0 |
| | Ice V | – | 156 | 134 | 48 | 0 | 0 |
| | Ice VI | – | 441 | 446 | 448 | 394 | 278 |
| | $R_{mantle}$ | – | 1803 | 1799 | 1798 | 1796 | 1795 |
| | $R_{core}$ | – | 709 | 715 | 714 | 719 | 723 |
| | S/Si | – | 5.38 | 6.21 | 7.45 | 8.72 | 10.09 |
| 10 | $q_b$ | 4 | 4 | 5 | 6 | 11 | 44 |
| | Ice Ih | 148 | 129 | 114 | 84 | 50 | 13 |
| | Liquid | 31 | 125 | 183 | 321 | 477 | 753 |
| | Ice III | 52 | 0 | 0 | 0 | 0 | 0 |
| | Ice V | 155 | 127 | 81 | 0 | 0 | 0 |
| | Ice VI | 447 | 465 | 475 | 460 | 348 | 130 |
| | $R_{mantle}$ | 1801 | 1788 | 1781 | 1769 | 1759 | 1738 |
| | $R_{core}$ | 713 | 730 | 741 | 759 | 772 | 799 |
| | S/Si | 5.57 | 7.73 | 9.18 | 12.30 | 15.84 | 21.67 |

reduces the thickness of the high-pressure ices. For example, if one takes a value only 1% larger, the thickness is reduced by 20%.

Ice III forms for lower-heat flow models with salinity greater than 3 wt%, owing to the freezing point suppression and low thermal expansivity of saline fluids. The effect could be even stronger for Cl-bearing fluids that have a stronger freezing point suppression. Expansivity and other thermodynamic data for those systems are not readily available for elevated pressure and temperatures below 273.15 K. For the $MgSO_4$ oceans considered here, salinities exceeding 5 wt% are denser than the ice phase, indicating that a transition from seawater-like frazil slurries to upward 'snow' could occur at Ganymede's seafloor as it cools. Based on the density profiles for the 10 wt% ocean shown in Fig. 4, a slightly higher salinity of ~12 wt% would result in flotation of ice V in a similar manner to that predicted for ice III. Buoyancy occurs over tens of kilometers, so the formation of frazil-like 'snows' could be a significant mechanism of heat transport analogous to precipitation of ice in Earth's atmosphere.

A frazil-snow transition is also indicated for the highest heat flux considered ($T_b = 270$ K) for the 10 wt% ocean. Recent phase measurements for the NaCl–$H_2O$ system, obtained by Journaux et al. (2013), provide a basis for comparison to assess whether this prediction is realistic. The ice VI transition occurring in our models at ~1600 MPa and 300 K (Table 1) occurs at a higher salinity of NaCl [4 mol $kg^1$ or 19 wt%; based on Figure 4 of Journaux et al., 2013]. Chloride suppresses the freezing temperature of water ice more effectively than sulfate under more modest pressures found in Earth's ocean. The stronger freezing point suppression predicted by our activity model suggests an error in the source data, as discussed in Section 3. Neglecting these uncertainties, the increasing silicate depth with salinity points to the possibility that the predicted 'snow' effects could happen at higher salinities where our models do not adequately predict thermodynamic behavior. Reproducing our model using the recent results for the NaCl system requires addressing gaps in the thermodynamic data for the aqueous phase above 500 MPa, as also noted by Journaux et al. (2013).

From the calculated mantle and core thicknesses we determine the mass fraction S/Si for Ganymede, as shown in Fig. 6, since this ratio can be compared with the terrestrial mass fraction S/Si = 0.0442 (Javoy, 1995) and the solar value of 0.522. Sulfur content of the core is determined by the core's size and our assumption of a eutectic FeS composition. Ocean thickness and sulfate composition determine the ocean's sulfur content. With no sulfur in the ocean, the ratio S/Si becomes the terrestrial value. This is merely a coincidence. The present model does not assume

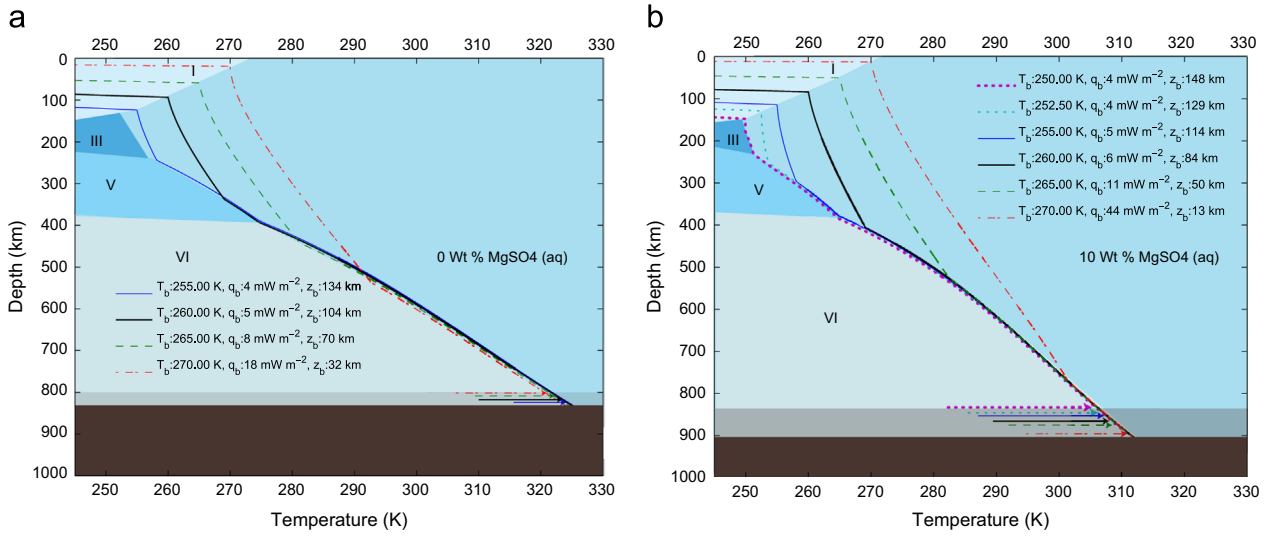


**Fig. 5.** Depths of fluid and ice layers in Ganymede for a pure water (a) and bulk 10 wt% $MgSO_4$ ocean (b), in km, based on temperature profiles shown for $T_b$ from 250 to 270 K. For the pure water case, Ice VI is the only high-pressure phase present when $T_b > 260$ K. Pressure is not uniform for the different curves because of varying amounts and densities of overlying materials. The melting temperature $T_b$ is not consistent with the high salt composition unless the ocean is compositionally stratified. Horizontal arrows for each value of $T_b$ indicate the radius of the silicate mantle computed based on Ganymede's mass and moment of inertia, which increases with $T_b$ for the pure water case but decreases for the 10 wt% case.

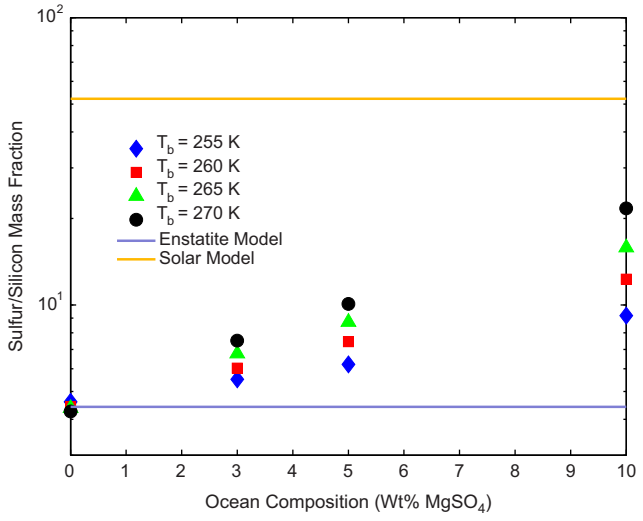


**Fig. 6.** Mass fraction sulfur relative to silicon in Ganymede based on our calculations of interior structure. We assume that sulfur fractionates entirely into an iron core containing 25 wt% sulfur as FeS, and into the ocean. S/Si is always far less than the solar value, but greater than or equal to the value predicted by the enstatite–chondrite model developed for Earth by Javoy (1995).

any sulfur in the silicate mantle. The proportion of sulfur in Ganymede's core is much larger than that in the Earth's core since the eutectic composition is assumed in the nominal model. If Ganymede's total sulfur approaches the solar value, there is enough sulfur for an ocean with 10 wt% $MgSO_4$(aq). The ability for Ganymede to extract this much sulfur into its ocean depends on the extent of water–rock interaction during Ganymede's formation.

## 6. Conclusions

We predict Ganymede's interior structure for representative oceans composed of aqueous magnesium sulfate. Our results suggest phenomena of geophysical, oceanographic, and astrobiological interest. Our simple activity model for the $H_2O$–$MgSO_4$ system reproduces melting curves at pressures and temperatures occurring in the interiors of large icy satellites. Applying this in combination with new thermodynamic data for the fluid phase constrains the thickness of Ganymede's ice I upper layer to between 13 km and 144 km in the absence of solid state convection. $MgSO_4$ ocean concentrations of up to 10 wt% lead to oceans as thick as 750 km, depending on internal heat flux. Ganymede's density structure constrains the radius of its iron core and silicate mantle consistent with those of the overlying materials.

Melting all of the high pressure ices requires ocean concentrations exceeding 10 wt%, which are buoyantly stable relative to ice VI at the interface between ice VI and rock. For the lowest heat flux values, ice III forms in the presence of liquids with salinity greater than 3 wt%. Ice phases III and VI are buoyantly unstable relative to the overlying liquid for salinities greater than 5 wt% and 10 wt%, respectively, leading to the prediction of upward 'snow'. Higher salinities are likely to result in similar behavior for ice V. Assessing equilibrium configurations in these scenarios requires accounting for heat transport from Ganymede's interior, including convective heat transport in salty oceans and high pressure ices, and partitioning of salts between the high pressure ices and upper and lower liquid layers.

Large uncertainties in Ganymede's moment of inertia strongly affect models of the interior structure. Investigations by the JUICE mission will address this issue (Grasset et al., 2013). Variations in ocean salinity also clearly influence the structure of Ganymede's interior. Understanding these influences in ways that can be interpreted through data from JUICE and other missions requires further experimental investigations into the thermodynamics and rheology of aqueous solutions and solids under relevant extremes of pressure encountered in Ganymede's interior.

## Acknowledgments

This work was partially supported by NASA Outer Planets Research grants NNX08AQ51G and NNH12ZDA001N, and by the Icy Worlds node of NASA's Astrobiology Institute (08-NAI5-0021). The research was carried out at the Jet Propulsion Laboratory, California Institute of Technology, under a contract with the National Aeronautics and Space Administration.

## References


Anderson, J., Lau, E., Sjogren, W., Schubert, G., Moore, W., 1996. Gravitational constraints on the internal structure of Ganymede. Nature 384, 541–543.

Andersson, O., Inaba, A., 2005. Thermal conductivity of crystalline and amorphous ices and its implications on amorphization and glassy water. Phys. Chem. Chem. Phys. 7, 1441–1449.

Barr, A., Pappalardo, R., Stevenson, D., 1781. Rise of deep melt into Ganymede's ocean and implications for astrobiology. In: Lunar and Planetary Institute Science Conference Abstracts, vol. 32, p. 1781.

Bland, M., Showman, A., Tobie, G., 2008. The production of Ganymede's magnetic field. Icarus 198, 384–399.

Bland, M., Showman, A., Tobie, G., 2009. The orbital-thermal evolution and global expansion of Ganymede. Icarus 200, 207–221.

Brown, M., Hand, K., 2013. Salts and radiation products on the surface of Europa. Astron. J. 145, 110.

Carlson, R., Calvin, W., Dalton, J., Hansen, G., Hudson, R., Johnson, R., McCord, T., Moore, M., 2009. Europa's surface composition. Europa. University of Arizona Press, Tucson, pp. 283–327.

Cassen, P., Peale, S.J., Reynolds, R.T., 1980. On the comparative evolution of Ganymede and Callisto. Icarus 41, 232–239.

Choukroun, M., Grasset, O., 2010. Thermodynamic data and modeling of the water and ammonia-water phase diagrams up to 2.2 GPa for planetary geophysics. J. Chem. Phys. 133, 144502.

Dalton, J., Shirley, J., Kamp, L., 2012. Europa's icy bright plains and dark linea: exogenic and endogenic contributions to composition and surface properties. J. Geophys. Res.: Planets (1991–2012) 117.

Fei, Y., Bertka, C.M., Finger, L.W., 1997. High-pressure iron–sulfur compound, $Fe_3S_2$, and melting relations in the Fe–FeS system. Science 275, 1621–1623.

Fortes, A., Choukroun, M., 2010. Phase behaviour of ices and hydrates. Space Sci. Rev. 153, 185–218.

Fortes, A.D., Wood, I.G., Knight, K.S., 2008. The crystal structure and thermal expansion tensor of $MgSO_4$–$11D_2O$ (meridianiite) determined by neutron powder diffraction. Phys. Chem. Miner. 35, 207–221.

Grasset, O., Mevel, L., Mousis, O., Sotin, C. 2001. The pressure dependence of the eutectic composition in the system $MgSO_4$–$H_2O$: implications for the deep liquid layer of icy satellites. In: Lunar and Planetary Institute Science Conference Abstracts, vol. 32, p. 1524.

Grasset, O., Dougherty, M., Coustenis, A., Bunce, E., Erd, C., Titov, D., Blanc, M., Coates, A., Drossart, P., Fletcher, L., Hussmann, H., Jaumann, R., Krupp, N., Lebreton, J.-P., Prieto-Ballesteros, O., Tortora, P., Tosi, F., Hoolst, T.V., 2013. JUpiter ICy moons Explorer (JUICE): an ESA mission to orbit Ganymede and to characterise the Jupiter system. Planet. Space Sci. 78, 1–21.

Grindrod, P., Fortes, A., Nimmo, F., Feltham, D., Brodholt, J., Vočadlo, L., 2008. The long-term stability of a possible aqueous ammonium sulfate ocean inside Titan. Icarus 197, 137–151.

Grover, J., 1977. Chemical mixing in multicomponent solutions: an introduction to the use of Margules and other thermodynamic excess functions to represent non-ideal behaviour. In: Thermodynamics in Geology. Springer, D. Reidel Publishing Company, Dordrecht-Holland, pp. 67–97.

Hauck II, S.A., Aurnou, J.M., Dombard, A.J., 2006. Sulfur's impact on core evolution and magnetic field generation on Ganymede. J. Geophys. Res. 111, E09008.

Hogenboom, D.L., Kargel, J.S., Ganasan, J.P., Lee, L., 1995. Magnesium sulfate-water to 400 MPa using a novel piezometer: densities, phase equilibria, and planetological implications. Icarus 115, 258–277.

Hussmann, H., Spohn, T., 2004. Thermal-orbital evolution of Io and Europa. Icarus 171, 391–410.

Javoy, M., 1995. The integral enstatite chondrite model of the Earth. Geophys. Res. Lett. 22, 2219–2222.

Journaux, B., Daniel, I., Caracas, R., Montagnac, G., Cardon, H., 2013. Influence of NaCl on ice VI and ice VII melting curves up to 6 GPa, implications for large icy moons. Icarus 226, 355–363.

Khurana, K., Kivelson, M., Stevenson, D., Schubert, G., Russell, C., Walker, R., Polanskey, C., 1998. Induced magnetic fields as evidence for subsurface oceans in Europa and Callisto. Nature 395, 777–780.

Kirk, R., Stevenson, D., 1987. Thermal evolution of a differentiated Ganymede and implications for surface features. Icarus 69, 91–134.

Kivelson, M., Khurana, K., Volwerk, M., 2002. The permanent and inductive magnetic moments of Ganymede. Icarus 157, 507–522.

Martin, W., Baross, J., Kelley, D., Russell, M., 2008. Hydrothermal vents and the origin of life. Nat. Rev. Microbiol. 6, 805–814.

McFadden, L.-A., Weissman, P., Johnson, T., 2007. The Encyclopedia of the Solar System. Elsevier.

McKinnon, W., 2006. On convection in ice i shells of outer solar system bodies, with detailed application to Callisto. Icarus 183, 435–450.

Melosh, H.J., Ekholm, A.G., Showman, A.P., Lorenz, R.D., 2004. The temperature of Europa's subsurface water ocean. Icarus 168, 498–502.

Nakamura, R., Ohtani, E., 2011. The high-pressure phase relation of the $MgSO_4$–$H_2O$ system and its implication for the internal structure of Ganymede. Icarus 211, 648–654.

Poirier, J.-P., 1994. Light elements in the Earth's outer core: a critical review. Phys. Earth Planet. Inter. 85, 319–337.

Poirier, J., Sotin, C., Peyronneau, J., 1981. Viscosity of high-pressure ice VI and evolution and dynamics of Ganymede. Nature 292, 225–227.

Schubert, G., Hussmann, H., Lainey, V., Matson, D., McKinnon, W., Sohl, F., Sotin, C., Tobie, G., Turrini, D., Van Hoolst, T., 2010. Evolution of icy satellites. Space Sci. Rev. 153, 447–484.

Showman, A., Stevenson, D., Malhotra, R., 1997. Coupled orbital and thermal evolution of Ganymede. Icarus 129, 367–383.

Soderlund, K., Schmidt, B., Wicht, J., Blankenship, D., 2014. Ocean-driven heating of Europa's icy shell at low latitudes. Nat. Geosci. 7, 16–19.

Sotin, C., Tobie, G., 2004. Internal structure and dynamics of the large icy satellites. C. R. Phys. 5, 769–780.

Šrámek, O., Ricard, Y., Bercovici, D., 2007. Simultaneous melting and compaction in deformable two-phase media. Geophys. J. Int. 168, 964–982.

Tobie, G., Grasset, O., Lunine, J.I., Mocquet, A., Sotin, C., 2005. Titan's internal structure inferred from a coupled thermal–orbital model. Icarus 175, 496–502.

Travis, B., Palguta, J., Schubert, G., 2012. A whole-moon thermal history model of Europa: impact of hydrothermal circulation and salt transport. Icarus 218, 1006–1019.

Vance, S., Brown, J., 2005. Layering and double-diffusion style convection in Europa's ocean. Icarus 177, 506–514.

Vance, S., Brown, J., 2013. Thermodynamic properties of aqueous $MgSO_4$ to 800 MPa at temperatures from −20 to 100°C and concentrations to 2.5 mol $kg^{-1}$ from sound speeds, with applications to icy world oceans. Geochim. Cosmochim. Acta 110, 176–189.

Vance, S., Goodman, J. 2009, Oceanography of an Ice-Covered Moon, In: Europa. Arizona University Press, Tucson, pp. 459–482.

Vance, S., Harnmeijer, J., Kimura, J., Hussmann, H., de Martin, B., Brown, J.M., 2007. Hydrothermal systems in small ocean planets. Astrobiology 7, 987–1005.

Yayanos, A.A., 2001. Deep-sea piezophilic bacteria. Methods Microbiol. 30, 615–637.

Zolotov, M.Y., Kargel, J., 2009. On the chemical composition of Europa's icy shell ocean and underlying rocks. In: Pappalardo, R.T., McKinnon, W.B., Khurana, K. (Eds.), Europa. University of Arizona Press, Tucson, AZ, pp. 431–458.